Preliminary 3D Analysis of the Heliospheric Response to the 28 October 2003 CME Using SMEI White-Light Observations

B. V. Jackson, A. Buffington, P. P. Hick, X. Wang

Center for Astrophysics and Space Sciences, University of California at San Diego, LaJolla, CA, U.S.A.

D. Webb

Institute for Space Research, Boston College, Chestnut Hill, MA

Short title: ANALYISIS OF THE 28 OCTOBER 2003 CMEs FROM SMEI

Abstract The Solar Mass Ejection Imager (SMEI) has recorded the inner heliospheric response in white-light Thomson scattering to the 28 October 2003 CME. This preliminary report shows the evolution of this particular event in SMEI observations, as we track it from a first measurement at approximately 20° from the solar disk until it fades in the anti-solar hemisphere in the SMEI 180° field of view. LASCO coronagraph images show a CME and an underlying bright ejection of coronal material that is associated with an erupting prominence. Both of these are seen by SMEI in the interplanetary medium. We employ a 3D reconstruction technique that derives its perspective views from outward-flowing solar wind to reveal the shape and extent of the CME. This is accomplished by iteratively fitting the parameters of a kinematic solar wind density model to both SMEI white-light observations and Solar-Terrestrial Environment Laboratory (STELab), interplanetary scintillation (IPS) velocity data. This modeling technique separates the true heliospheric signal in SMEI observations from background noise and reconstructs the 3D heliospheric structure as a function of time. These reconstructions allow separation of the 28 October CME from other nearby heliospheric structure and a determination of its mass. The present results are the first utilizing this type 3D reconstruction with the SMEI data. We determine an excess-over-ambient mass for the southward-moving ejecta associated with the prominence material of 7.1×10^{16} g and a total mass of 8.9×10^{16}g. Preliminary SMEI white-light calibration indicates that the total mass of this CME including possible associated nearby structures may have been as much as $\sim 2.0 \times 10^{17}$ g spread over much of the Earthward-facing hemisphere.

1 Introduction

The 28 October 2003 CME was, by all standards, an exceptional solar event. The initial CME shock response took 19.4 hours to reach Earth [Cliver et al, 2004], one of the fastest recorded transit times to date[1]. The Solar Mass Ejection Imager (SMEI) [*Eyles et al.,* 2003, *Jackson et al.,* 2004] measures Thomson-scattered sunlight with a broadband spectral response viewing most sky globally around the Earth. SMEI successfully recorded all-sky images at this time, except for an ~1 day outage beginning at ~0 UT 30 October 2003 just after the bulk of the CME event arrived at Earth.
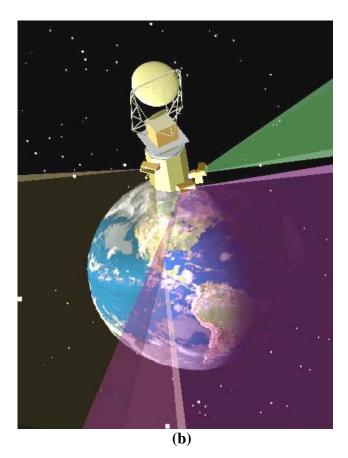
---

[1] The fastest CME shock response to date on record on 4-5 August, 1972 traveled from Sun to Earth in a brief 14.6 hours [Cliver *et al.*, 1990].

SMEI was launched January 6, 2003 on the Air Force Space Test Program satellite Coriolis (Figure 1). Using a combination of 3D modeling and image analysis techniques, the SMEI observations can quantify the 3D extents of transient and corotating heliospheric structures and their interactions with each other and slow-moving ambient solar wind. Precisely calibrated SMEI images are required for displaying typical slow and fast-moving heliospheric structures in 2D sky maps and for their 3D reconstructions.

In this article we use the term "CME" to include various aspects of a sequence beginning with the ejection of material from the corona that moves outward into the heliosphere. In this paper we show first-time SMEI results. From the heliospheric SMEI data alone it is impossible to separate the original coronal material forming the mass ejection as it is observed by coronagraphs from the ambient coronal and heliospheric material affected ('swept up') by the passage of the CME. Thus, the term CME in the context of this paper is used to describe a process that includes both the 'original' CME ejecta and the induced responses in the outer corona and heliosphere (where it is observed by SMEI).

Section 2 briefly describes the UCSD 3D analysis techniques used here to analyze SMEI data. These techniques, and results presented here for the first time with SMEI data, include the 3D solar wind reconstructions that in turn provide enhanced SMEI sky maps of the 28 October CME as well as a series of 3D views displaying outward motion for different portions of the CME. Section 3 presents the results of these analyses, locations, volumes and masses of the CME. We conclude in Section 4.

Figure 1. (a) The Coriolis spacecraft with the Solar Mass Ejection Imager (SMEI) on board prior to launch from Vandenberg AFB. The three SMEI camera baffles (circled) are seen on the lower portion of the spacecraft. The *Windsat* antenna is at the top. **(b)** SMEI in its terminator polar orbit at 840 km with an orbital inclination of 98°. SMEI looks away from the Earth at 30° above the local horizontal to avoid sunlight reflected from the Earth and from the *Windsat* antenna. The fields of view of the three cameras (each shown as shaded wedges extending from the satellite) together cover nearly 180° of sky, and as the instrument orbits Earth, sweep out nearly the whole sky around it.

2   SMEI Analysis Techniques

2.1   *UCSD SMEI Data Frame Processing*

Telemetry data from SMEI are relayed from the ground stations to the Air Force Research Laboratory (AFRL) data processing center at Hanscom Air Force Base, Boston.   There data packets are concatenated, the individual CCD camera data frames are decompressed and combined with spacecraft pointing information derived from a star tracker. The resulting data

frames arrive at UCSD via an internet file transfer process (FTP).[2] At UCSD we maintain a database of these SMEI data frames in near real time on a local server. Our colleagues at Sacramento Peak also maintain an archive of original SMEI data, and display orbit-by-orbit SMEI sky map differences in near real time for public viewing.

The UCSD analysis sequence processes individual SMEI data frames to produce a heliospheric sky map for every orbit of data. These maps retain the original 0.2° SMEI angular resolution and are optimized for photometric accuracy. Briefly, we:

1. Identify and remove corrupted and saturated data frames;

2. Remove the electronic offset, subtract a dark-current contribution and perform geometrical optical and flat field corrections for each frame;

3. Register the photometric measurements onto a standard sidereal coordinate frame;

4. Remove cosmic-ray particle and space-debris contributions and combine ~1500 frames from each camera to form an all-sky map for each orbit; and finally

5. Convert the resulting sidereal map as desired to different coordinate projections – sidereal or sun-centered; fisheye, or all-sky Hammer-Aitoff.

Additional detail about this part of the analysis is found in *Jackson et al*. [2004].

Since light from the sidereal sky (stars, the Milky Way, bright nebulae and galaxies) is much brighter than the variable heliospheric Thomson-scattered signal, contributions from these must be subtracted from the orbital sky maps. The simplest way to remove this background is by subtracting Sun-centered sky maps from orbits adjacent in time ('running differences'); a constant heliospheric signal present in both orbits cancels in the difference map, so in effect only the <u>change</u> in the heliospheric signal over the orbital time period, $\Delta t = 102$ minutes, is measured. *Tappin et al.* [2004] used this method to display observations of the heliospheric response to a
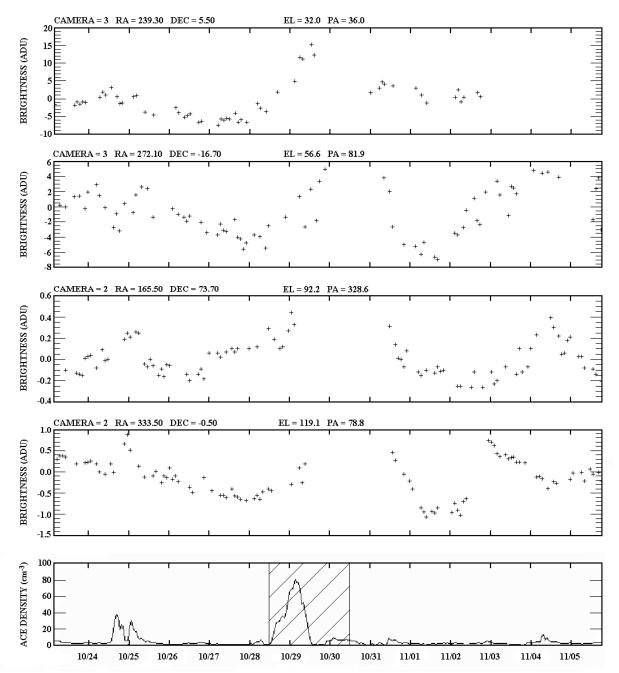
---

[2] Hanscom also derives "pipeline processing" all-sky images for each orbit, with a coarser angular and photometric resolution. These are useful for detecting many CMEs and are available to the public in near real time at http://smei.nso.edu/index.html.

halo CME that originated on the Sun on 28 May 2003, and was observed by SMEI on 29 May. More than 140 such events have been observed in the SMEI data to date by this method; of these, about half were likely associated with CMEs observed in the SOHO LASCO coronagraph data. [*Webb et al.*, in preparation].

Alternatively, a sidereal sky map averaged over orbits covering many days close to the heliospheric event can be subtracted from the orbits containing the event itself. This method preserves more of the heliospheric signal by effectively enlarging the time scale Δt to many days, and is the method used in the present analysis. In addition, we have removed a zodiacal cloud brightness by fitting an analytic model to these data in a Sun-centered reference frame. The removal of this signal minimizes large changes with time of background light from this source, especially near the Sun. The basic data used here for 3D reconstruction consists of photometric timeseries at selected sidereal line-of-sight sky locations. To avoid possible contributions from bright or variable stars, analysis is further restricted to those lines of sight farther removed than 1.5° from any star brighter than sixth magnitude. To remove unwanted trends over time due to incompletely removed zodiacal light, background light or long-term instrument variation, each line of sight has a running mean baseline of about one week duration removed from it. We conclude that this current UCSD analysis provides a stable baseline over time scales of several weeks without sacrificing angular resolution: this is sufficient for analyzing transient heliospheric disturbances and the 3D reconstructions presented here.

Figure 2 presents a sample time series from the ~1100 sky locations used for the present analysis of the October 2003 data. These were selected from an original group of ~4000 evenly spaced sidereal locations, each averaged to include one square degree of sky. Brightness for these data is given in camera analog-to-digital units (ADU). A natural unit for surface brightness in the present work is "S10", the equivalent of the brightness of a tenth magnitude star spread over one square degree of sky. Preliminary calibration of the data (to an accuracy of about 10%)

using 'G-star' brightnesses observed in a prototype SMEI camera operated on the ground gives 1 S10 = 0.55 ADU. These time series are edited to remove auroral light. Bright aurora at heights above 840 km were discovered unexpectedly by SMEI [*Jackson et al.,* 2004; *Mizuno et al*., 2004]. Their contributions are removed by editing the time series. Auroral light is present only at times when SMEI passes through the auroral ovals.   For the 28 October 2003 event the aurora onset time occurs when the CME impacted Earth. To remove the aurora, SMEI time series sequences are displayed in time and by orbit. Those data points that are contaminated by auroral light as recognized by orbit location, and time, are deleted from the time series by an automatic procedure that first cuts abrupt brightness value changes above limits impossible for CME signals, and then deletes any remnant of the signal to the edge of this deletion in location and time. The ~1100 time series in turn produce approximately 80,000 valid lines of sight over a two-week interval centered on the CME arrival at Earth. The 80,000 number is sufficiently redundant to support a 3D reconstruction having a $6.7° \times 6.7°$ latitude and longitude digital resolution and half-day temporal cadence. The analysis converges to a solution within a few hours (see next section).

Figure 2. **(top)** A sample of time series for 195 SMEI orbits from 23 October − 5 November 2003 from one square degree sky bins at the RA, Dec. and also at the 12 UT 29 October position angles and elongation locations indicated. A large brightness enhancement is first seen at the end of the day on 28 October in these sequences, especially nearest the Sun. The disturbance shows as a broad peak persisting more than a day. **(bottom)** The ACE *in situ* solar wind density time series (hourly averages) shows that the enhancement reaches Earth early 29 October, and continues well into the day. The ACE density rise on 28-29 October occurs has been revised [Skoug *et al.*, 2004], and is no longer thought to be as large as shown in these early measurements.

8

2.2   3D Reconstruction Analysis

Solar physics has seen numerous attempts to reconstruct the structure of the corona and the heliosphere in three dimensions. In particular, these techniques have been developed for coronal mass ejections in order to understand the physical principles of their initiation. Employing techniques different from those used here, *Munro* [1977], *Crifo et al.* [1983] and *MacQueen* [1993] analyzed views from the Earth perspective using Thomson-scattering data. *Jackson et al.* [1985], using Helios photometer and Solwind coronagraph views from different perspectives, determined the approximate dimensions and surface origins of CMEs. *Jackson and Hick* [1994] and *Jackson and Froehling* [1995], using Helios photometer and Solwind coronagraph views from different perspectives and tomographic techniques, analyzed CMEs and mapped their 3D shapes.

Rotational tomography of stationary solar structures (streamers) using coronagraph observations were attempted by *Wilson* [1977], *Jackson* [1977], and more recently by *Zidowitz et al.* [1995] and *Frazin and Janzen* [2002]. Using both Helios 1 and Helios 2 photometer measurements, *Hick and Jackson* [1998] and *Jackson and Hick* [2000; 2002] fit photometric observations to a kinematic heliospheric model that incorporates both solar rotation and outward solar wind flow. The rotational tomographic analyses show that a significant enhancement in contrast between dense and less dense regions is achieved, especially during solar minimum.

Interplanetary scintillation (IPS) measurements have been used to probe solar wind features since the 1960's using ground-based meter-wavelength radio observations [*Hewish et al.*, 1964; *Houminer*, 1971]. Observations from the UCSD [*Coles and Kaufman*, 1978] and Nagoya [*Kojima and Kakinuma*, 1987] multi-site scintillation arrays have determined velocities in the interplanetary medium since the early 1970's. The IPS observations, resulting from a radio propagation effect caused by small-scale (~200km) density variations, track heliospheric

disturbances of larger scale that vary from one day to the next and are often associated with geomagnetic storms on Earth [*Gapper et al*., 1982]. These observations show a predominance of disturbances that corotate with the Sun as inferred from a list of events and their associations [*Hewish and Bravo*, 1986]. 3D results from IPS observations recorded over a wide range of elongations were obtained by least squares fitting to a heliospheric model incorporating both outward solar wind flow and solar rotation [*Jackson et al*., 1997; *Kojima et al*., 1997; *Jackson et al*., 1998; *Kojima et al*., 1998; *Asai et al*., 1998]. In the 3D models derived from IPS analysis, scintillation strength serves as a proxy for density. In the models in these earlier papers scintillation strength is related to a value of small-scale density variation that is in turn scaled to bulk density and solar distance using a set of power law relationships.

Early Helios photometer and IPS tomographic reconstructions assumed that the kinematic heliospheric model remains unchanged over a month-long time spanned by the observations. This implies that, within this time period, the heliospheric structures remain unchanged except for outward radial expansion and solar rotation as described by the kinematic modeling. Current UCSD tomographic modeling [*Jackson et al.,* 2001; 2002 and *Jackson and Hick*, 2004] relaxes this assumption, and a kinematic solar wind model formed at regular time intervals is iterated to provide the 3D heliospheric parameters used to fit observed data. This article reports on application of this modeling technique to SMEI data for the first time.

2.3   Computational Analysis

The computational aspects of the 3D reconstruction program [see *Jackson et al.,* 1998 and *Hick and Jackson*, 2003, and references therein for a more mathematical derivation of this process] necessarily include the detailed geometry for each line of sight: the location of each within the 3D solar wind model and its projection to a source surface reference level below all lines of sight. In the present tomographic analysis scheme, Carrington maps at evenly spaced time intervals at this source surface provide boundary conditions for a 3D velocity and density solar

wind model that propagates outward from this surface. The 3D solar wind model is integrated at

the location and time of each line of sight and compared with observations using a least-squares

technique. The line-of-sight segment projections in space and time to each source surface are

known from the modeling, and they are iteratively inverted in 2D space and time on these source

surfaces to update boundary conditions for the model to better fit observations.

In the least-squares process described above, ratios of model to observed values are

monitored at each iteration to indicate a rate of convergence. Here, velocity and density

corrections to the model are made separately. First, changes are made to previous velocity

boundary conditions on the reference surface. Secondly, the 3D model is updated and new

projected locations of each line-of-sight point on the reference surface are determined. This

assures that the newest values of velocity determine the 3D model and their projections back to

the source surface for each line of sight segment. Thirdly, changes are made to previous density

boundary conditions on the reference surface. Finally, the 3D model is again updated with all

the newest boundary values.

The source surface Carrington maps of velocity and density are smoothed on each

iteration using a 2D Gaussian spatial filter that incorporates equal solar surface areas, and a

Gaussian temporal filter. These filters are predicated by the numbers of lines of sight and noise

in the data and can be varied to ensure convergence. For these preliminary 28 October 2003

analyses, the reconstruction e^{-1} filter values have been set to spatial widths of 15° for the IPS

velocity data and 5° for SMEI data, and temporal widths of 0.75 and 0.325 days, respectively, for

IPS velocity and SMEI data.   The digital coordinate resolutions for both data sets are set

spatially to 6.7° × 6.7° heliographic latitude and longitude and to a half day temporal cadence to

approximately match the Gaussian filter resolution [see *Jackson and Hick*, 2004]. We require

the amplitude of the sum of all Gaussian contributions at a single coordinate position be more

than one in order that several different perspective lines of sight produce changes in the modeled

values. Where the sum of all contributors is less than one, in order to obtain continuity along lines of sight, the source surface value is interpolated from locations where the data can be changed. Where the values in the model cannot be changed at some location, these coordinate positions are left blank in the final result. For the 28 October CME event SMEI data, this includes a section of heliospheric volume within the hemisphere opposite Earth that cannot be observed and reconstructed by SMEI at the 6.7° spatial resolution scale.
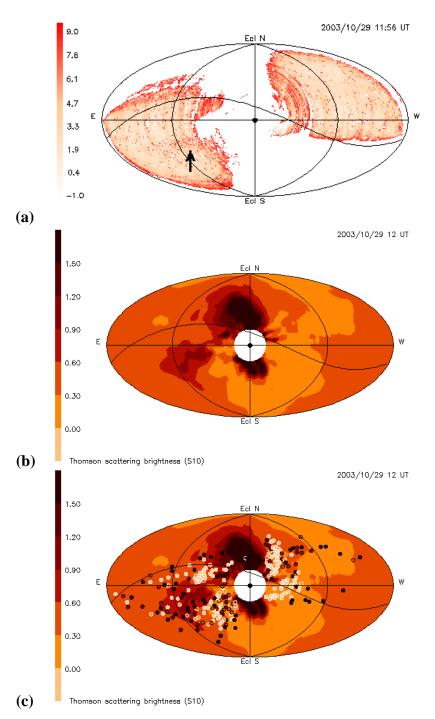
This program generally converges to an unchanging model within a few iterations. The program is set to operate for 9 iterations to be certain the program has converged [see *Jackson et al.*, 1998]. For a typical rotation and the digital resolutions above, a set of density and velocity iterations generally takes about a half hour on a 1.5 GHz Pentium IV computer. Those IPS velocity observations and SMEI brightness lines of sight throughout the period that do not fit within a three-sigma limit of the mean ratio change ascribed at that location by the model are removed from the data set. The program then operates for another 9 iterations. We find that the model solutions are insensitive to the starting model values, and after a few iterations any signature of the initial model is lost. Other tests [see *Jackson et al.*, 1998] show that tomographically analyzing a set of artificial observations using a known 3D input reproduces the input.

3   Analysis Results

3.1   Sky Maps

Figure 3a shows a SMEI Hammer-Aitoff sky map just as the 28 October 2003 CME arrives at Earth midday on 29 October. Figure 3a combines one orbit's worth of approximately 4500 individual $3° \times 60°$ data frames from all three SMEI cameras. The brightness scale to the left of the map is in ADU (Section 2.1). A portion of the sky map is blanked out and not shown in the figure where too many high-energy particle hits (cosmic rays) and auroral light produce an

apparent response far above the background. Figure 3b is a sky map resulting from the above-described 3D reconstruction using the full set of time series (Figure 2 examples). The brightness scale is in S10. The resulting S10 scale of Figure 3b is about a factor of 10 smaller than the ADU scale of Figure 3a. In spite of data outages in individual maps from particle hits, aurora, and an outage for most of 30 October, more than enough information remains in the time-series sequences to reconstruct several portions of the 28 October CME, and render visible low-contrast heliospheric features difficult to see in individual sky maps. These include part of the CME to the northeast of the Sun, not much evidence of a solar halo of bright material elsewhere, and another bright structure ejected to the south. Additional bright material in these sky maps to the southeast in Figure 3b is probably associated with an earlier series of bright CMEs observed by LASCO midday 26 October and early 27 October.
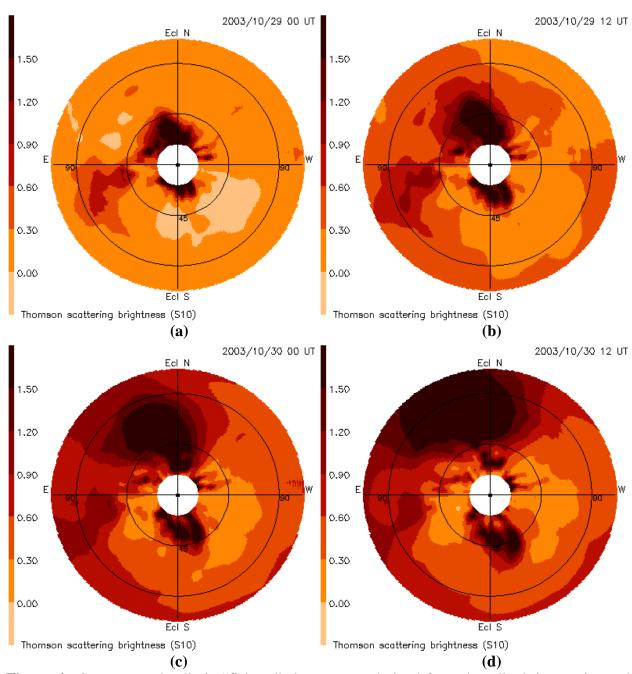
(a)

(b)

(c)

Figure 3. Sun-centered Hammer-Aitoff sky maps of the October 28, 2003 CME as viewed from SMEI. The faster portion of the CME directed towards Earth lies primarily to the solar northeast and begins to engulf Earth (reaching 90° elongation) over the whole of the map at this time. The large prominence-associated ejecta to the south of the Sun have reached about 45° elongation. The brightness scale of each map is placed to the left. **a)** A direct single-orbit sky map compiled from ~ 4500 SMEI data frames. The time series of Figure 2 are located on the map at the data frame observation time with the beginning time indicated on the map. Brightness is in ADU. Large portions of the map are blanked out by high-energy particle hits and auroral light. An arrow indicates a CME structure in the direct map image. **b and c)** Sky maps as derived by the edited time series and 3D reconstructions fit to the direct images of the event as it moves outward from the Sun over the period of one day. The locations of all valid time series positions within a 102-minute period of 12 UT 29 October are positioned on (c). These maps have an r^{-2} heliospheric density normalized to unity at 90° elongation as a radial filter multiplier.

14

Few other remote-sensing heliospheric observations of this series of events exist. The STELab, Japan IPS observations [*Tokumaru et al,* 2004] map little data to the south at this time of year, and thus missed most of the eruption of the large southward-directed prominence-associated ejecta. The IPS scintillation level response does, however, show an enhancement primarily to the solar northeast and little to the west, consistent with SMEI data.
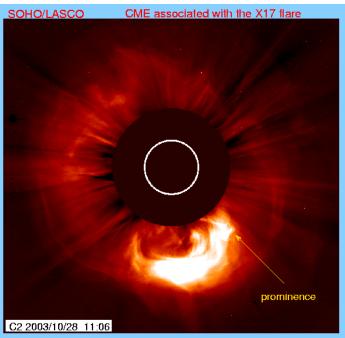
3.2 3D Reconstruction

Figures 4a – d present a sequence of "fisheye" sky maps similar to Figure 3b and 3c, and show the progression of the CME outward in 2D sky maps. The sky maps are derived from the density volumes that have been fit to the observed data by integrating through the volumes and summing the total line of sight brightness Billings [1965]. The volumes have an r^{-2} heliospheric density normalized to unity at 90° elongation as a radial filter multiplier. Thus, the sky maps from them better show the outward progression of heliospheric structures both before and interpolated to the middle of the one-day data outage that began at ~0 UT 30 October. In addition, these sky maps from the tomographic modeling have a 5 $e^{-}cm^{-3}$ base removed from them, and thus present excursions from a mean of zero much as the time series of Figure 2. Because the fit to a heliospheric solar wind model uses time series from multiple sky maps, and helps remove signals that do not participate in the outward progression of the solar wind, bad spots in the data can be filled in to provide continuous coverage. In addition, since few unwanted signals remain, the scale of the map excursions can be enhanced above those of direct sky maps, and thus far more detail can be discerned in them. This analysis shows not only the bright heliospheric CME response primarily to the solar northeast that engulfs the Earth, but also details of the large prominence and white-light eruption first observed in the LASCO coronagraph (Figure 5). This moves outward into the heliosphere and passes south-southeast of the Earth. An earlier slower-moving disturbance to the solar southeast that began its outward motion on about 0 UT 27 October 2003 is also seen in this sky map sequence.
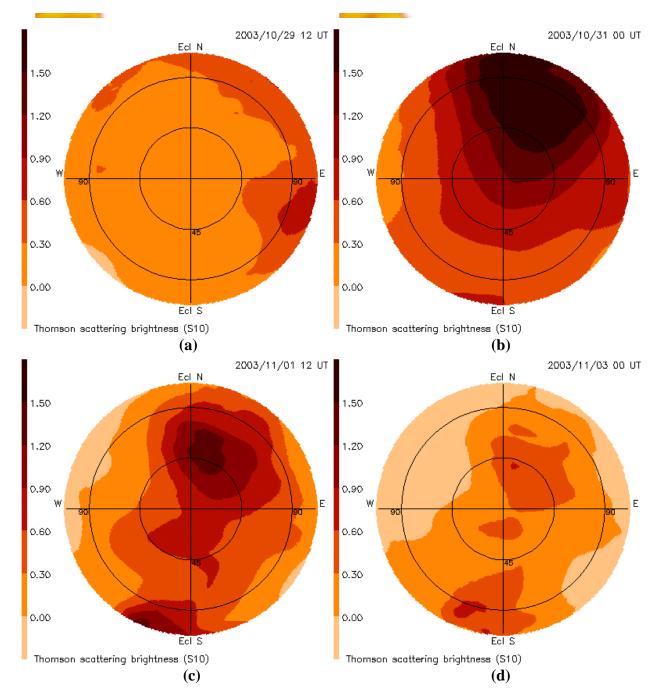
15

Figure 4. Sun-centered ecliptic "fisheye" sky maps as derived from the edited time series and 3D reconstructions. These are shown out to 110° elongation as viewed from SMEI for the October 28, 2003 CME as it moves outward from the Sun over a period of two days. These maps have an r^{-2} heliospheric density normalized to unity at 90° elongation as a radial filter multiplier so that CME features can be more directly compared as they move outward. **a-d)** The faster portion of the CME directed towards Earth lies primarily to the solar northeast and begins to engulf Earth (reach 90°) about midday on October 29. At the same time the large prominence-associated ejecta to the south of the Sun has reached just beyond 45° elongation. Different CME portions can be observed to move outward over the next two sky maps. Since there are no data from SMEI midday 30 October 2003, the presentation at time **(d)** is a model interpolation resulting from the time series data on either side of the gap in SMEI observations.

16

The 3D density distribution from which these sky maps were derived allow results to be viewed from any vantage-point, not just from Earth. Determination of the 3D structure has the advantage of more completely allowing more complete measurement of the directions of travel of heliospheric structures over time and their masses since several objects often overlap in the 2D views. Figures 6a-d show a 3D reconstruction of this CME at four times as a remote observer would view the event from 30° above the ecliptic plane

Figure 5. LASCO C2 observations of the October 28, 2003 CME. Most of the early CME response 'halos' the Sun and is associated with an X17.2 flare at S16 E09 that commences at 10:36 UT October 28. The large eruption to the south associated with a solar prominence (indicated) is also viewed to move outward over time to the south in LASCO images.

and about 45° west of the Sun-Earth line. Only the portion of the heliosphere volume on the earthward side of the sun plus or minus about 110° relative to Earth in longitude is depicted in this reconstruction. The 3D resolution is presently limited by the numbers of lines of sight used in the analysis, here far fewer than will ultimately be available. Even so, these reconstructions show that the fast portion of the CME engulfing Earth was far more extensive and dense to the solar northeast than in other directions. The analysis also shows that a portion of the connected density structure extends back to near the prominence ejection, and that the prominence begins to break up into separate pieces in the inner heliosphere. Better views of the direction of travel of these features are shown in another set of fisheye sky maps that are centered on the anti-solar direction (Figure 7a-d). Here, the fast portion of the CME vanishes to the solar northeast while ejecta associated with the prominence move off to the solar southwest. The line-of-sight

17

Figure 7. Fisheye sky maps of the October 28, 2003 CME directed 180º from the Sun. **a-d)** Sky maps as derived by the edited time series and 3D reconstructions shown at intervals of one and a half day. Figure 6a has the same time in common with Figure 3, Figure 4b, and Figure 5b and includes some of the same structure since these maps extend to 110° from the center. The bulk of the portion of the CME that engulfed Earth fades away at about 45º from the Sun-Earth line.

observations producing these sky maps are more numerous towards sun, but also provide a good

sampling within the area covered by the original maps. Thus, Figure 7 maps may not correspond

as closely to the direct sky maps in this direction of space, as would an average including all the line-of-sight observations.

3.3 CME Mass

In these analyses we assume one electron is associated with 2.0×10^{-24}g of mass, a combination of 10% helium ions and 90% hydrogen ions [*Hildner et al.,* 1975]. The CME mass derived for this event is made up of two portions that include an ambient that is swept up and moved outward by the large pulse of energy input to the lower corona, and a portion that was originally heliospheric closer to the Sun and expelled during the event. Although we can not distinguish unambiguously between these two mass types from the SMEI analysis alone, we can model both with solar distance if we assume a standard heliospheric background ambient mass and, noting the location and volume of the CME structure, derive both a total and an excess mass for it. For ejecta associated with the prominence this modeling effort is not difficult since the structure is fairly isolated from the rest of the CME and has a reasonably well-defined shape. We determine values for two portions of this structure at a contour level (30 e$^-$cm^{-3}) where they become well separated. The core of the first (or "**a**") portion of this structure in Table 1 lies nearly parallel to the observer's line of sight, is somewhat more dense than the other, and its near end is closer to Earth. The second ("**b**") portion (see Figure 8) spreads over a large range of longitudes and its center moves outward about 70º from the sun-earth line. As for excess and total mass, it is not possible to tell what portion of the ejecta is associated solely with Hα prominence material, but in all likelihood the denser portion of the "**a**" structure retains some of the shape and material of this originally less-ionized material.
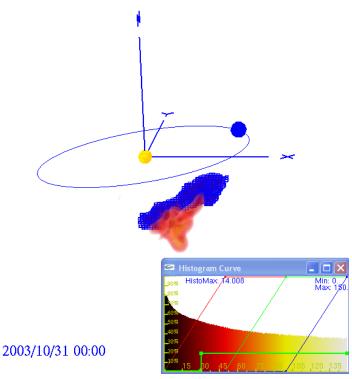
Table 1 lists the masses obtained for various parts of this CME. Determinations of mass are made at two different times as the material moves outward as a check on the technique. The CME structure close to the Sun is better defined, but contains less volume for accurate measurement: thus, unless otherwise noted, measurements at both times should be given equal

19

weight. The earthward-directed structure moves more rapidly than the southward-directed component, so measurements of the latter are necessarily obtained later in time when it has reached greater distances from the Sun. Table 1 names the structure measured in the first column. The reconstruction times for the measured structures are given in columns 2 and 6. The volume of the structure is limited by a 3D contour set so that except for the third entry (Total CME excluding previous west event) the structure is isolated from others. These contour levels are given in column 3 and column 7 of Table 1. Excess and total mass at the different times for these structures are given in columns 4 and 5 and 8 and 9 respectively. We show more significant figures for mass than accuracy might warrant in order to display differences between excess and total mass. Accuracies vary with structure and most include a host of modeling factors and potential systematic error such as residual auroral and uncertainty in the SMEI brightness calibration. These modeling factors and systematic errors affect both the mass and the lower contour interval, and we expect the present masses to be no more accurate than ~20%.

Table 1. 3D CME masses derived for the 28 October 2003 CME.

	1st Recon. Time	Lower Contour (e^-cm^{-3})	Excess Mass ($\times 10^{16}$g)	Total Mass ($\times 10^{16}$g)	2nd Recon. Time	Lower Contour (e^-cm^{-3})	Excess Mass ($\times 10^{16}$g)	Total Mass ($\times 10^{16}$g)
Earth-directed density	29 Oct. 12 UT	10.0	6.7	8.3	30 Oct. 0 UT	10.0	6.9	8.6
Total CME	29 Oct. 12 UT	10.0	13.6	16.9	30 Oct. 0 UT	10.0	14.0	17.2
Total CME excluding previous west event	29 Oct. 12 UT	4.0	~12.3	~16.8	30 Oct. 0 UT	4.0	~15.1	~20.5
Prominence-associated ejecta - **a**	30 Oct. 0 UT	30.0	0.77	0.88	31 Oct. 0 UT	30.0	0.70	0.80
Prominence-associated ejecta - **b**	30 Oct. 0 UT	30.0	1.45	1.61	31 Oct. 0 UT	30.0	1.51	1.69
Prominence-associated ejecta total	30 Oct. 0 UT	10.0	7.10	8.81	31 Oct. 0 UT	10.0	7.11	8.93

Since few other papers in the literature detail this method of determining heliospheric mass [*e.g.*, *Wang et al.*, 2003] the technique used here is demonstrated in Figure 8 for an example structure (the fourth entry, or "**a**" portion of the prominence-associated ejecta on 0 UT 31 May). A 3D contour level is set to isolate the mass of the structure from others, and cubes that occupy the volume within the contour then approximate the heliospheric structure. The sum of the mass within these cubes determines the total mass of the structure, and the summed volume of the cubes gives the heliospheric volume of the structure. By assuming an ambient solar wind (we here use a value of 5 e⁻

Figure 8. Mass measurement of the prominence-associated ejecta **a** portion of the May 28 CME (highlighted in blue) as described in the text. The view is from about 20° north of the ecliptic plane, and 110° east of the Sun-Earth line. Dense foreground portions of the CME (see Figure 5) have been removed by cutting planes leaving this portion of the event easy to view. Part of the more southward **b** portion of the prominence ejecta lies below and in front of the highlighted **a** portion from this viewpoint. The insert to the lower right of the figure gives a histogram of the number of volume elements at different densities, their colors, and the selected lower contour level at 30 e⁻cm⁻³. The total mass highlighted in the table is 8×10^{15}g and the volume is 0.014 AU³ (see Tables 1 and 2).

cm⁻³ at 1 AU with an r⁻² falloff as used for the 3D reconstruction), we obtain a value of excess mass above the ambient within this contour as a difference of the total mass and the ambient.

Table 2 gives more information about the 28 October 2003 CME from the 3D reconstructions. Here each structure is again listed, followed by its reconstruction time in column 2. Column 3 gives the lower contour interval used to define the structure, the same as for the values in Table 1. Structure centroid location and upper and lower limits are given

21

respectively by three numbers: height in AU, and ecliptic latitude and longitude in degrees relative to Earth (east minus, west plus). Measurement errors are generally about 0.01 AU and a few degrees. Occasionally the reconstructed structure lies outside of the volume SMEI can view. In this case the "measurements" are tomographic extrapolations and presumed less accurate than values where there was a direct view, and these values are marked. The inner boundary source surface was chosen to be at 15Rs. The Table 2 centroid locations are probably more accurately determined by these analyses than the volumes and structure extents since the latter depend not only upon the assumptions inherent in the kinematic modeling, but also on the location of the lower contour interval from the SMEI brightness calibration that currently has a precision of ~10%.

Table 2. 3D CME volumes and location for the 28 October 2003 CME.

	1st Recon. Time	Lower Contour (e^-cm^{-3})	Volume (AU^3)	Centroid (AU, deg.)	Upper Limit (AU, deg.)	Lower Limit (AU, deg.)	Lat. Extent (AU, deg.)	Long. Extent (AU, deg.)
Earth-directed density	29 Oct. 12 UT	10.0	0.226	0.70 +30 -5	1.13 0 0	0.31 50 0	130	90
Total CME	29 Oct. 12 UT	10.0	0.308	0.70 +30 -5	1.13 0 0	0.17* -70* 10*	170	205
Total CME excluding previous west event	29 Oct. 12 UT	3.5	0.860	0.70 +30 -5	1.14 0 0	0.17* -70* 10*	180	205
Prominence-associated ejecta - **a**	30 Oct. 0 UT	30.0	0.014	0.67 -40 25	0.80 -40 15	0.41 -55 55	40	75
Prominence-associated ejecta - **b**	30 Oct. 0 UT	30.0	0.015	0.56 -75 15	0.81 -75 20	0.35 -75 10	30	200
Prominence-associated ejecta total	30 Oct. 0 UT	10.0	0.119	0.56 -75 15	0.87 -75 20	0.30 -75 20	70	205

* values extrapolated from later times

4 Conclusion

White-light Thomson scattering observations from SMEI have recorded the inner heliospheric response to the 28 October 2003 CME. This paper shows the extent of the CME in SMEI observations, and we are able to track the event from its first measurement approximately 20° from the solar disk until it vanishes from the SMEI field of view on the side of earth opposite the sun. Several portions of the CME can be followed into the interplanetary medium associated with the initial CME response and the underlying erupting prominence structure. The present work is the first application of UCSD 3D tomography to the photometric SMEI data, and these preliminary results are very encouraging. The technique obtains perspective views of outward-flowing solar wind and allows separating the heliospheric response from other sources of background noise, filling in regions of missed or noisy data, and determining the 3D structure of the CME and estimating its mass. The analysis shows details of the CME as it evolves outward past Earth, but is preliminary because significantly improved results both in photometric precision and angular resolution will be available as we further refine the SMEI analysis algorithms and include more lines of sight. Also, more sophisticated 3D modeling techniques will hopefully refine observational fits to the data.

References

Asai, K., M. Kojima, M. Tokumaru, A. Yokobe, B.V. Jackson, P.L. Hick, and P.K. Manoharan (1998), Heliospheric tomography using interplanetary scintillation observations, 3. Correlation between speed and electron density fluctuations in the solar wind, *J. Geophys Res.*, *103*, 1991.

Billings, D.E. (1966), A guide to the solar corona, Academic, New York, p. 150.

Cliver, E. W., J. Feynman, and H.B. Garrett (1990), An estimate of the maximum speed of the solar wind, 1938-1989, *J. Geophys Res.*, 95, 17,103.

Cliver, E.W., *Solar Phys.* (submitted)

Coles, W. A., and J.J. Kaufman (1978), Solar wind velocity estimation from multi-station IPS, *Radio Science 13*, 591.

Crifo, F., J.P. Picat, and M. Cailloux (1983), Coronal transients: Loop or bubble?, *Solar Phys.*, *83*, 143.

Eyles, C.J., G.M. Simnett, M.P. Cooke, B.V. Jackson, A. Buffington, P.P. Hick, N.R. Waltham, J.M. King, P.A. Anderson, and P.E. Holladay (2003), The Solar Mass Ejection Imager (SMEI), *Solar Phys.*, *217*, 319.

Frazin, R.A., and P. Janzen (2002), Tomography of the solar corona. II. Robust, regularized, positive estimation of the three-dimensional electron density distribution from LASCO-C2 polarized white-light images, *Astrophys. J., 570*, 408.

Gapper, G.R., A. Hewish, A. Purvis, and P.J. Duffett-Smith (1982), Observing interplanetary disturbances from the ground, *Nature 296*, 633.

Hewish, A., and S. Bravo (1986), The sources of large-scale heliospheric disturbances, *Solar Phys. 106*, 185.

Hewish, A., P.F. Scott, and D. Wills (1964), Interplanetary scintillation of small diameter radio sources, *Nature*, *203*, 1214.

Hick, P., and B.V. Jackson (1998), Three-dimensional tomography of heliospheric features using Thomson-scattering data, *Proc. SPIE*, *3442*, 87.

Hick, P.P., and B.V. Jackson (2003), Heliospheric tomography: an algorithm for the reconstruction of the 3D solar wind from remote sensing observations, *Proc. SPIE, San Diego*, 7-8 August 2003, *5171*, 287.

Hildner, E., J.T. Gosling, R.M. MacQueen, R.H. Munro, A.I. Poland, and C.L. Ross (1975), The large coronal transient of 10 June 1973 I: observational description, *Solar Phys.*, *42*, 163.

Houminer, Z. (1971), Corotating plasma streams revealed by interplanetary scintillation, *Nature Phys. Sci., 231*, 165.

Jackson, B.V. (1977), A coronal hole equatorial extension and its relation to a high speed solar wind stream, Topical Conference on Solar and Interplanetary Physics, Tucson, Arizona, January 12-15, 7.

Jackson, B.V., and P.L. Hick (1994), Three dimensional reconstruction of coronal mass ejections, in the proceedings of the Third SOHO Workshop on Solar Dynamic Phenomena & Solar Wind Consequences, *ESA SP-373*, 199.

Jackson, B.V. and H.R., Froehling (1995), Three-dimensional reconstruction of a coronal mass ejection, *Astron. Astrophys.*, *299*, 885.

Jackson, B.V. and P. Hick (2000), Three dimensional tomography of heliospheric features using global thomson scattering data, *Adv. in Space Res.*, *25(9)*, 1875.

Jackson, B.V. and P.P. Hick (2002), Corotational tomography of heliospheric features using global Thomson scattering data, *Solar Phys.*, *211*, 344.

Jackson, B.V. and P.P. Hick (2004), Three-dimensional tomography of interplanetary disturbances, in: Solar and Space Weather Radiophysics Current Status and Future Developments, D.G. Gary and C.U. Keller (eds.), *ASSL 314*, Kluwer, The Netherlands, 355.

Jackson, B.V., R.A. Howard, N.R. Sheeley, Jr., D.J. Michels, M.J. Koomen, and R.M.E. Illing (1985), Helios spacecraft and Earth perspective observations of three looplike solar mass ejections, *J. Geophys. Res*., *90*, 5075.

Jackson, B.V., P.L. Hick, M. Kojima and A. Yokobe (1997), Heliospheric tomography using interplanetary scintillation observations, *Adv. Space Res*., *20* (1), 23.

Jackson, B.V., P.L. Hick, M. Kojima, and A. Yokobe (1998), Heliospheric tomography using interplanetary scintillation observations, 1. Combined Nagoya and Cambridge observations, *J. Geophys. Res*., *103*, 12,049.

Jackson B.V. A. Buffington A., and P.P. Hick (2001), A heliospheric imager for solar orbiter, in Proc. of "Solar Encounter: The First Solar Orbiter Workshop, Puerto de la Cruz, Tenerife, Spain, 14-18 May 2001 (*ESA SP-493)*, 251.

Jackson, B.V., P.P. Hick, and A. Buffington (2002), Time-dependent tomography of heliospheric features using the three-dimensional reconstruction techniques developed for the Solar Mass Ejection Imager (SMEI), *Proc. SPIE, Waikoloa*, 22-28 August 2002, *4853*, 23.

Jackson, B.V., A. Buffington, P.P. Hick, R.C. Altrock, S. Figueroa, P. Holladay, J.C. Johnston, S.W. Kahler, J. Mozer, S. Price, R.R. Radick, R. Sagalyn, D. Sinclair, G.M. Simnett, C.J. Eyles, M.P. Cooke, S. J. Tappin, T. Kuchar, D. Mizumo, D.F. Webb, P. Anderson, S.L. Keil, R. Gold, and N.R. Waltham (2004), The Solar Mass Ejection Imager (SMEI) mission, *Solar Phys.* (in press).

Kojima, M., and T. Kakinuma (1987), Solar-cycle evolution of solar-wind speed structure between 1973 and 1985 observed with the interplanetary scintillation method, *J. Geophys. Res., 92*, 7269.

Kojima, M., K. Asai, P.L. Hick, B.V. Jackson, M. Tokumaru, H. Watanabe, and A. Yokobe (1997), Solar wind structure at 0.1-1 AU reconstructed from IPS observations using tomography, in: Robotic Exploration close to the Sun: Scientific Basis, edited by S.R. Habbal, *AIP Conference Proceedings 385*, 97.

Kojima, M., M. Tokumaru, H. Watanabe, A. Yokobe, K. Asai, B.V. Jackson, and P.L. Hick (1998), Heliospheric tomography using interplanetary scintillation observations, 2. Latitude and helioocentric distance dependence of solar wind structure at 0.1-1 AU, *J. Geophys. Res.*, *103*, 1981.

MacQueen, R.M. (1993), The three-dimensional structure of 'loop-like' coronal mass ejections, *Solar Phys.*, *145*, 169.

Mizuno, D.R., A. Buffington, M.P. Cooke, C.J. Eyles, P.P. Hick, P.E. Holladay, B.V. Jackson, J.C. Johnston, T. Kuchar, J.B. Mozer, S. Price, R.R. Radick, G.M. Simnett, D. Sinclair, and D.F. Webb (2004), Very high-altitude aurora observations with the Solar Mass Ejection Imager, *J. Geophys. Res.,* submitted.

Munro, R.H. (1977), Coronal transients: arches or bubbles?, Topical Conference on Solar and Interplanetary Physics, Tucson, Arizona, January 12-15, 10.

Skoug, R.M., J.T. Josling, J.T. Steinberg, D.J. McComas, C.W. Smith, N.F. Ness, Q. Hu, and L.F. Burlaga (2004), Extremely high speed solar wind: 29-30 October 2003, *J. Geophys Res.,* *109*, A09102.

Tappin, S.J., A. Buffington, M.P. Cooke, C.J. Eyles, P.P. Hick, P.E. Holladay, B.V. Jackson, J.C. Johnston, T. Kuchar, D. Mizuno, J.B. Mozer, S. Price, R.R. Radick, G.M. Simnett, D. Sinclair,

N.R. Waltham, and D.F. Webb (2004), Tracking a major interplanetary disturbance with SMEI, *Geophys. Res. Lett.* , *31*, L02802.

Tokumaru, M., M. Kojima, K. Fujiki, M. Yamashita, and D. Baba (2004), Interplanetary consequences caused by the extremely intense solar activity during October-November 2003, *J. Geophys Res*. (submitted).

Wang, X., P.P. Hick, B.V. Jackson, and M. Bailey (2003), Visualization of remotely-sensed heliospheric plasmas for space weather applications, *Proc. SPIE, San Diego*, 7-8 August 2003, *5171*, 280.

Wilson, D.C. (1977), *NCAR Cooperative Thesis No. 40*, Ph.D. thesis to the University of Colorado, Boulder, Colorado.

Zidowitz, S., B. Inhester, and A. Epple (1995), The three-dimensional structure of the solar corona, in *Solar Wind Eight*, *AIP Conference Proceedings 382*, edited by D. Winterhalter, J.T.Gosling, S.R. Habbal, W.S. Kurth, and M. Neugebauer, pp. 165-168, Woodbury.